Jurnal Kejuruteraan 36(5) 2024: 1859–1873
https://doi.org/10.17576/jkukm-2024-36(5)-07

Development of Plasma Probe Platform for In-situ Measurement with Real-time Communication System Using Sounding Rocket

Zulkifli Abdul Aziz & Siti Harwani Md. Yusoff*

School of Aerospace Engineering Engineering Campus,
Universiti Sains Malaysia, Malaysia

**Corresponding author: aeharwani@usm.my*

Received 9 February 2024, Received in revised form 6 June 2024
Accepted 6 July 2024, Available online 30 September 2024

ABSTRACT

This paper presents the development of a plasma probe platform designed for in-situ measurements, complemented by a real-time communication system. The primary objective is to establish an integrated system that seamlessly merges a plasma probe platform with a dependable and efficient real-time communication infrastructure. The platform is equipped with a diverse array of sensors, including those for temperature, magnetic field, acceleration, camera imaging, pressure, and GPS positioning. This comprehensive sensor suite enhances our comprehension of the intricate relationship between in-situ plasma probe measurements and various environmental parameters. The real-time communication system plays a pivotal role in ensuring continuous and uninterrupted data transmission between the platform and the ground station operator throughout the data collection process. This enables valuable real-time access to the gathered data, facilitating immediate analysis and decision-making. Moreover, the real-time communication system serves as a fail-safe mechanism in case of recovery failure, guaranteeing that data can still be transmitted and monitored even if the platform encounters difficulties during retrieval. By adopting this integrated approach, researchers gain the capability to monitor, analyze, and derive insights from the collected data in real-time, even under challenging recovery scenarios. The development of this advanced plasma probe platform, coupled with the effective real-time communication system, significantly enhances our capacity to investigate plasma phenomena. These advancements hold substantial implications for space exploration, atmospheric research, and a wide range of scientific endeavors, paving the way for groundbreaking discoveries and advancements in our understanding of complex physical phenomena.

Keywords: Mesosphere; ionosphere; plasma; in-situ measurement; plasma probe

INTRODUCTION

The Earth's atmosphere is formed by layers of gases that insulate it from cosmic rays and extraterrestrial radiation. This protective layer also regulates the Earth's temperature by acting as a thermal blanket. The five primary layers of the atmosphere are troposphere, stratosphere, mesosphere, thermosphere, and exosphere. The mesosphere, the third layer and the thickest at 35 km runs from approximately 50 to 85 km above the Earth. It is the coldest portion of the Earth's atmosphere with temperatures ranging from -2°C to -92°C, owing to the Mesosphere's decreased air density, less heat is absorbed, resulting in a cooler temperature. Carbon dioxide (CO^2) molecules also contribute to the layer's cooling impact by collecting heat energy and releasing light (Meriwether & Gerrard, 2004).

The mesosphere is the most complicated layer to examine, and comparatively less is known about it than other layers. Weather balloons and commercial aircraft are unable to reach it, while satellites orbiting below 100 km cannot maintain their orbit, leaving sounding rockets as the sole viable alternative. Recent research has demonstrated that the Mesosphere's ions can provide crucial information on natural phenomena such as seismic activity and space weather, indicating that there is still more to learn about this enigmatic layer (Liu et al. 2020; Shiro et al. 2012).

The exploration of electrons in the ionosphere layer has become increasingly fascinating due to extensive research conducted through various methods such as

ground-to-space measurements (using a sounding system and optical system) or in-situ measurements using a sounding rocket (Latif et al. 2020; Mahoudian et al. 2020; Yao et al. 2013). Each of these methods has its advantages and disadvantages. Ground measurement is advantageous in terms of cost and allows for an unlimited number of data collection (Ejiri et al. n.d.); however, the data need to be calibrated and verified using in-situ measurement and are limited to only a single type of data, i.e., measurement of electron density. On the other hand, in-situ data measurement can provide a better understanding by linking up multiple sensors that could lead to a single outcome (Amatucci et al. 2001; Mahoudian et al. 2020). Despite these methods, the mesosphere atmosphere layer remains poorly understood. Little study has been done due to the limited access time available at this altitude for in-situ measurement. Moreover, the cost and opportunity to launch a sounding rocket have also become significant factors.

Thus, this paper will focus on the development of a reliable platform that can accurately calibrate and verify in-situ measurements of electron density in the mesosphere and ionosphere layer allowing for a more comprehensive and continuous collection of data that can be used to study the activity and characteristics of these atmospheric layers.

SYSTEM OVERVIEW

The system overview is divided into two phases. In Phase 1, the Preliminary Analysis and Design Process begins by defining the instrument's objective to classify broad objectives and constraints and estimate quantitative development needs and requirements. The design concepts and architectures are then characterized to identify system drivers, ultimately meeting the objectives. The design is evaluated by identifying critical requirements and component selection trade-offs, establishing the baseline design concept. Finally, the design requirements are well defined, including system requirements and allocating system elements' requirements to the schematic design and simulation.

In Phase 2, the Manufacturing, Assembly, Integration, and Test process involves assembling various components, from individual pieces to subsystems, to form a complete system. During the initial period of manufacturing and testing, researchers prepare engineering data, complete drawings, and supporting information such as bills of materials, part specifications, and processing methods. The manufacturing components process is divided into four stages: manufacturing planning, component procurement, component assembly, and acceptance testing. Following the component assembly process, the qualifying phase begins, during which functional tests and environmental exposure are conducted.

SYSTEM DESCRIPTION

Development of Plasma Probe platform for In-situ Measurement will be designed to be operated in between 50-100 km orbit for at least 10 minutes. The system should be designed to be compatible with most RH-200 sounding rockets as a baseline (Noga & Puri, 2020). The system shall weigh less than 5 kg.

Table 1 describes the project system hierarchy, divided into two segments: space and ground. The space segment focuses on system development, including the main platform and payloads, and categorizes each subsystem and its components. The ground segment includes the mission control system, the user interface for communicating with the space segment in orbit. This segment outlines the components needed for seamless communication between ground and space.

TABLE 1. System hierarchy

Segment	Element	Subsystems	Components
Space Segment	Platform	Structure & Mechanical	Structure
		Thermal	Flexible Polyimide Heater
		Command and Data Handling	Onboard Computer, Memory, Real-time Clock, Flight Operating System
		Electrical Power	DC-DC Converter, Battery Pack
		Telecommunication	TransceiverAntenna
		Sensor	Magnetometer, Accelerometer, Pressure, Temperature, GPS
	Main Payload	Plasma Probe	Plasma probe
	Secondary Payload	Imaging	CMOS VGA
Ground Segment	Mission Control	Antenna & RF Subsystem	Antenna system, Transceiver

SYSTEM REQUIREMENTS

Table 2 is crucial to enable the successful deployment and operation of the system in the mesosphere and ionosphere environment. The instrument is designed to operate within an altitude range of 50-100 km and a temperature range of room temperature down to -92°C (Meriwether & Gardner, 2000). The primary objective of the instrument is to support a plasma probe as the primary payload (Latif et al. 2020), while the secondary objective is to collect data from all sensors, including imagery. The instrument is required to survive the harsh environment of the atmosphere and during launch. In addition, the instrument must be designed to be compatible with the volume and mass limitations of a sounding rocket, as it is intended to be hosted as a payload (Christe et al. 2016).

The system requirements determine all subsystem requirements and specifications. The system design is constrained by the requirements and specifications to perform the mission. The main constraints are volume and mass.

The structural volume and mass limitations of the system are derived from the example of a two-stage rocket that can reach up to a maximum altitude of 70 km namely RH-200. RH-200 is a series of sounding rockets developed by the Indian Space Research Organisation (ISRO) for meteorological and atmospheric study (Kim et al. 2020; Uma et al. 2024).

During mission and conceptual design study, it is recognized that payload volume constraints the capacity of payload (or experiment) that it carries. The design needs to meet all system requirements; with the available volume and mass to dedicate for all instrument subsystems, i.e., on-board computer, batteries, communications, sensors, actuators, payloads, and structure.

To ensure that all subsystems could fit within the allocated volume, significant decisions had to be made. It was recognized that the antenna for the communication subsystem, the plasma probe, and the harnessing were crucial components that required accommodation. To reduce the complexity of physical wire harnesses and assembly, a strategy similar to the CubeSat standard was adopted, which involves stacking subsystems using the PC104 connector (Nieto-Peroy & Emami, 2019). To comply with the requirement that the plasma probe be exposed to space for efficient data gathering, it was combined with the main structure to minimize its weight. Due to the limited space available, a whip antenna was found impractical, and a passive deployment mechanism was deemed necessary.

TABLE 2. System requirements

ID	Requirement	Descriptions
SR01	Orbital	Design for operation within the altitude range of 50-70 km
SR02	Temperature	Design to operate within a temperature range of room temperature down to -92°C
SR03	Primary Objective	Support primary payload i.e., Plasma probe
SR04	Secondary Objective	The system shall have the capability to support collecting all sensor data including the image
SR05	Survivability	The system shall survive the harsh environment in Mesosphere and Ionosphere, and during launch
SR06	Volume and Mass	The system shall be designed to be able hosted as a payload in the sounding rocket
SR07	External Interface	The system-to-ground station interface shall satisfy the space-to-ground ICD
SR08	Internal Interface	The platform shall provide electrical, mechanical, and thermal interfaces required to support the payload.

SYSTEM DESIGN

OVERVIEW MISSION

Based on the mission diagram Figure 1, the overall mission overview involves launching a designed system carrying a Plasma probe and a secondary payload to perform in-situ measurements and capture images in the mesosphere layer between 50 and 70 km using a sounding rocket. The plasma probe will collect data during the payload in the ionosphere layer along with all other sensor data, including magnetic field, gyro, temperature, pressure, picture, and positioning. These sensors and payload data will be stored in the onboard memory and simultaneously transmitted to the ground via the onboard transmitter if required. Additionally, the system will be able to receive instructions from the ground to reset itself if necessary or to turn on/off specific sensors.

SYSTEM ARCHITECTURE

The system architecture is developed through the design stages, preliminary and detailed levels, as shown in Figure 2 below. It is a straightforward satellite bus architecture

with On-Board Computer (OBC) based on the ATmega2560 at the center hub connecting other subsystems including Electrical Power, Sensors, Actuators, Communications, and payloads. This system is to accommodate to carries two payloads: (1) Plasma probe, and (2) CMOS camera. The system is powered by a battery pack that is sufficiently operating the entire system during its mission period. Since the system is expected to operate for a short duration, the system is expected to operate with no back-up system or redundancy, and it will only be capable of operating in a single mission until the battery falls below its critical voltage. In this case, the battery will be fully charged before flying.

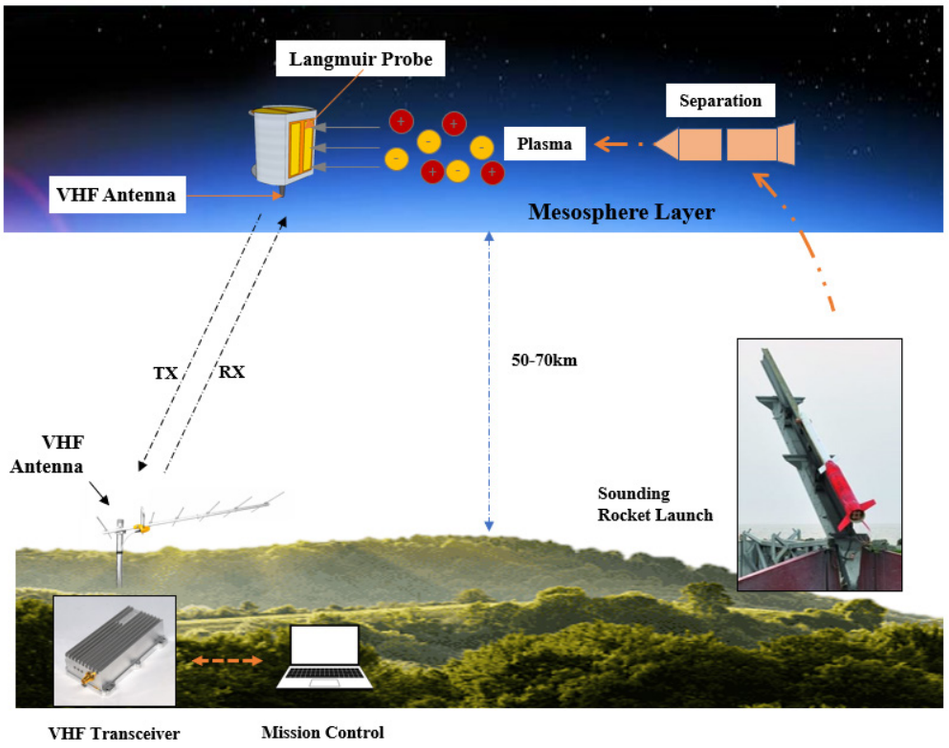

FIGURE 1. Overview mission diagram

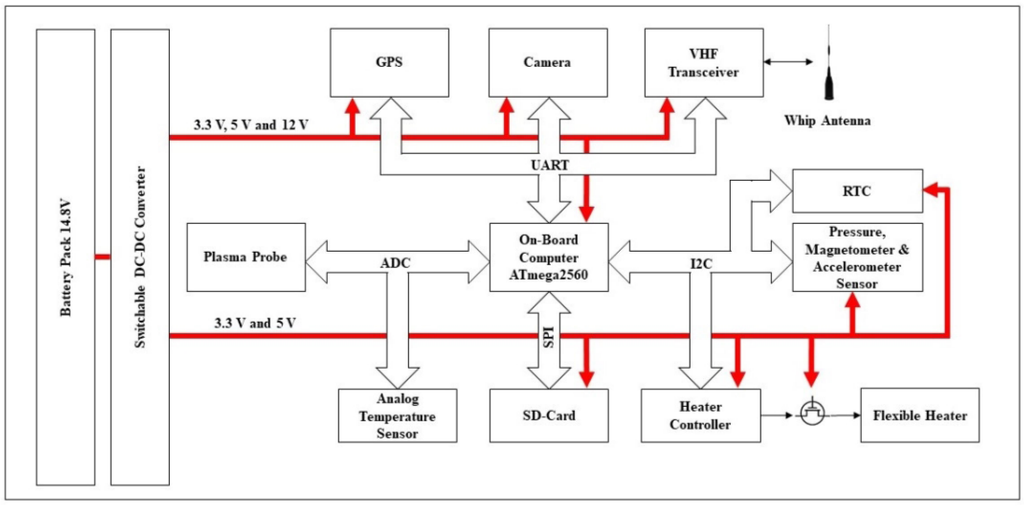

FIGURE 2. System architecture

The system is designed for rapid and low-cost integration, utilizing as many Commercial Off-The-Shelf (COTS) components or hardware as possible, while progressively developing in-house hardware in parallel.

To minimize physical connections and simplify integration, the system employs the PC104 connector, a widely used interface in CubeSats, facilitating vertical integration. Figure 3 and Figure 4 illustrate the location of each board and the integration process.

SYSTEM DESCRIPTION

Based on Figure 2 the designed OBC is based on ATmega2560 as its main microcontroller. It's a low-power Microchip 8-bit AVR® RISC-based microcontroller that executes powerful instructions in a single clock cycle. This allows it to strike a fine balance between power consumption and processing speed. Atmega2560 combines 256 KB ISP flash memory, 8 KB SRAM, 4 KB EEPROM, 86 general purpose I/O lines, 32 general purpose working registers, real-time counter, six flexible timer/counters with compare modes, PWM, four USARTs, byte-oriented Two-Wire serial interface, 16-channel 10-bit A/D converter, and a JTAG interface for on-chip debugging.

The device achieves a throughput of 16 million instructions per second (MIPS) at 16 MHz and operates between 4.5 and 5.5 volts. The block diagram of the ATmega2560 is shown in Figure 5 and the outcome of the Printed Circuit Board (PCB) of the main OBC shown in Figure 6.

The OBC operating system is based on a Real-Time Operating System (RTOS). RTOS is a reliable, flexible, and widely used real-time operating system that is well-suited for embedded systems and microcontroller-based applications. Its small footprint, advanced features, and ease of use make it suitable for this application (Amos 2020; Astafyeva 2019).

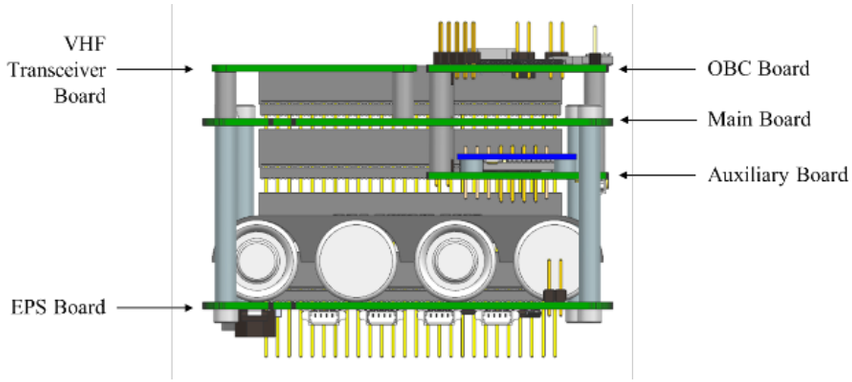

FIGURE 3. Mechanical assembly of the system

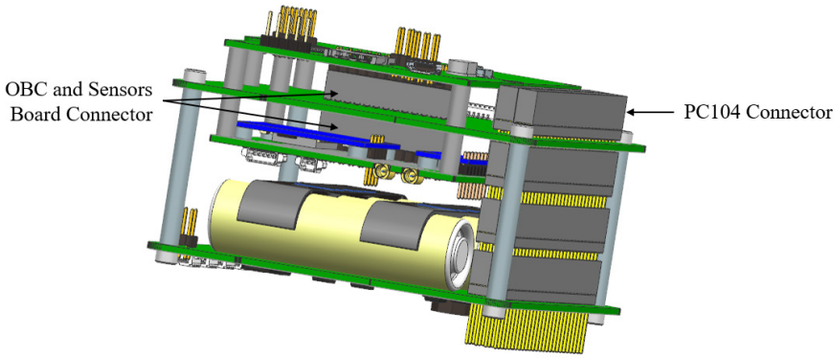

FIGURE 4. Interfaces via PC104 connector

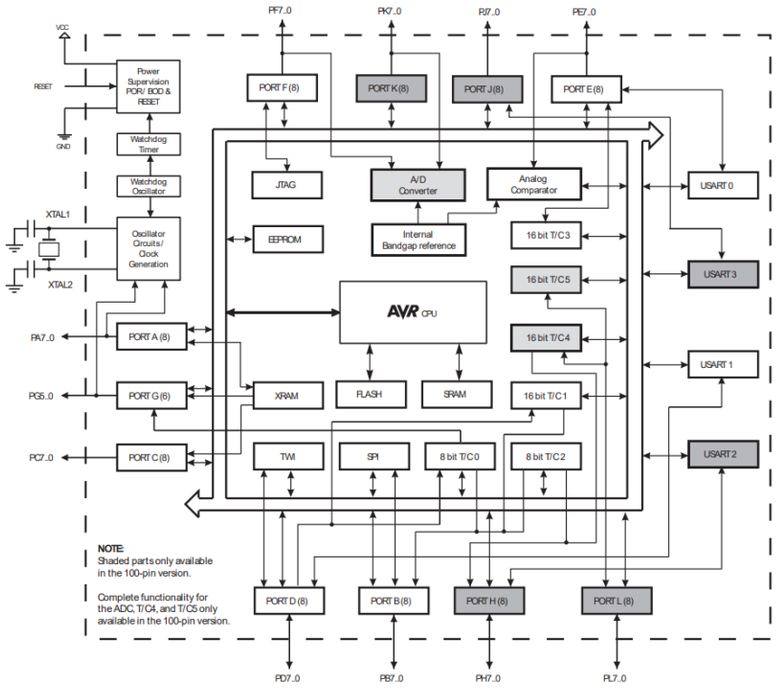

FIGURE 5. ATmega 2560 block diagram

As part of the command and data handling subsystem, the OBC will have a real-time clock (RTC) to track the current time and date, even when the system is off or rebooted. The RTC provides timestamps for data logging, event sequencing, and scheduling. The DS3231 from Maxim Integrated was chosen for this purpose due to its low cost and highly accurate I²C RTC with an integrated temperature-compensated crystal oscillator (TCXO) and crystal. The device incorporates a battery input and maintains accurate timekeeping when the main power to the device is interrupted (Ward, 2023).

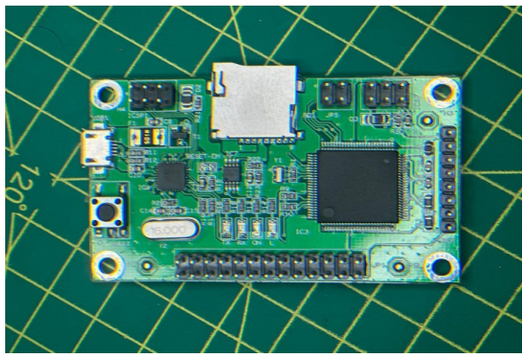

FIGURE 6. OBC based on ATmega 2560

Electrical power in this system powers the hardware and payloads onboard. The Electrical Power Subsystem (EPS) is critical, ensuring a reliable and continuous power source during the mission. The EPS generates, distributes, and regulates the power needed by other subsystems and payloads. It consists of batteries, power regulators, and distribution units.

The following in Table 3 outlines the expected power consumption for each subsystem and payload. It ensures the EPS can meet the peak power demands and optimize power consumption for effective mission performance. Assuming a 100% duty cycle is to cater for 10 minutes of mission operation.

The battery pack is based on 4 series and 1 parallel (4S1P) configuration. Each cell of the battery (see Figure 7) can provide a nominal capacity of 2600 mAh at 3.7 V. Thus, the maximum potential capacity of the battery pack is 9.62 Watt-hours (Wh).

FIGURE 7. 18650 Li-Ion Cell 2600 mAh

Based on Table 3, the energy consumption for 10 minutes of operation is 1.72 Wh, and the balance available upon completion of the mission is 7.89 Wh which is 82%

of the total capacity at the Beginning of Life (BOL) (Dahbi et al. 2017).

The EPS board is equipped with battery charger capability to charge the battery pack using 5V as input voltage via PC104. This charger design is based on the LT1513. LT1513 is an IC battery charger chip specifically optimized to use the Single-Ended Primary-Inductor Converter (SEPIC) converter topology

TABLE 3. System power budget

No	Component	Description	Duty Cycle (%)	Rated Power (W)	Sub-total (W)
1	Command & Data Handling	OBC, RTC and Memory	100	0.2	0.2
2	Thermal	Flexible Heater	50	18	9
3	Electrical Power	DC-DC Converter	100	0.2	0.2
4	Communication	VHF Transceiver – TX	50	1	0.5
		VHF Transceiver – RX	100	0.2	0.2
5	Camera	RGB Camera	10	0.4	0.04
6	Sensors	Magnetometer, Accelerometer, Temperature, GPS	100	0.2	0.2
		Total (W)			10.34

The SEPIC topology has unique advantages for battery charging. It will operate with input voltages above, equal to, or below the battery voltage, has no path for battery discharge when turned off, and eliminates the snubber losses of flyback designs.

As shown in Figure 8, the EPS board has three types of LDOs: two high current LDOs for 5 V and 3.3 V that can handle up to 1.2A, and six low current LDOs, including three for 3.3 V and three for 5 V. The LDOs can be controlled by the ground station operator or pre-programmed in the OBC. In addition to it, there is a sensor to monitor the temperature of the battery.

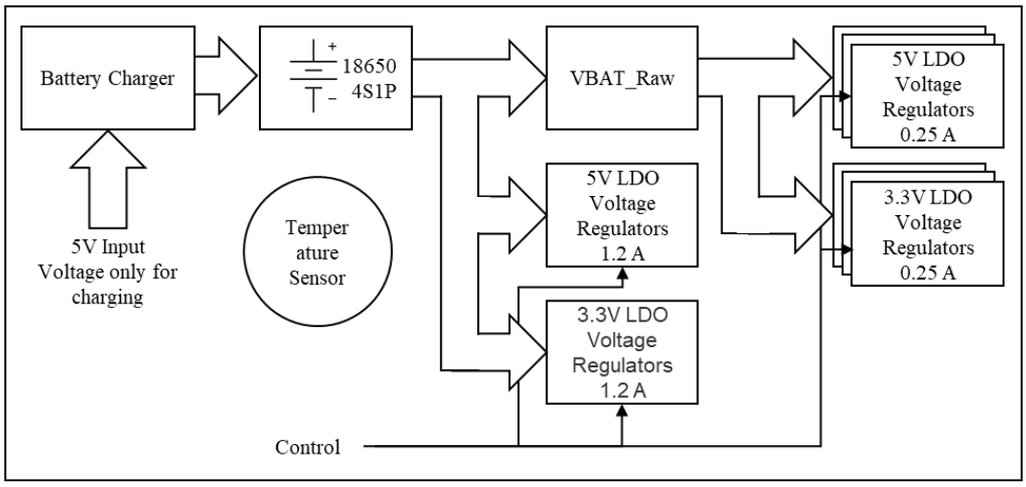

FIGURE 8. EPS block diagram

The mainboard, depicted in Figure 9 and Figure 10, plays a crucial role as the central interface connecting several key components within the system. It acts as a bridge between the On-Board Computer (OBC) board, EPS board, auxiliary board, and VHF Transceiver board. The primary function of the mainboard is to facilitate the exchange of data and power among these interconnected modules.

By serving as the central hub, the mainboard enables seamless communication and coordination between the various subsystems. It establishes the necessary electrical connections and data pathways, ensuring efficient data transfer and power distribution throughout the system.

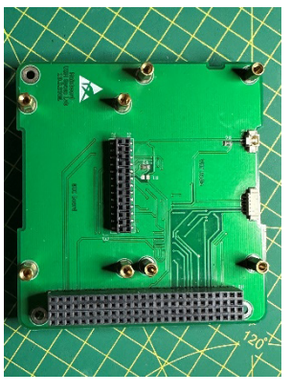

FIGURE 9. Mainboard top

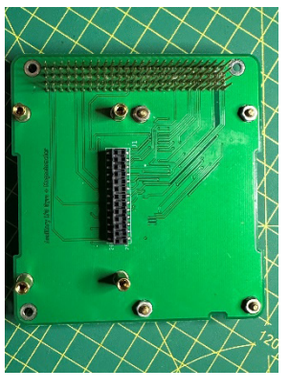

FIGURE 10. Mainboard bottom

While performing its crucial role as an interface, the mainboard itself does not contain any active components, except for an analog temperature sensor. This sensor is specifically designed to measure the temperature of the mainboard itself. By monitoring its temperature, the mainboard can ensure optimal performance and take necessary precautions to prevent overheating or other temperature-related issues.

The auxiliary board as shown in Figure 11 serves as a central platform that accommodates various sensors and facilitates the connection between the payloads, such as the camera and Plasma probe. Its primary function is to host and interface with these sensors, enabling data collection and integration with the main system. Two notable sensors included are:

1. GPS Board: This board integrates a Global Positioning System (GPS) module, which enables precise positioning and navigation. By leveraging satellite signals, the GPS board provides accurate location information that can be utilized for geolocation, tracking, and synchronization purposes. It enhances the system's ability to precisely determine its position in real-time, which is crucial for many applications.
2. Breakout Board: The breakout board combines two key sensor modules: a magnetometer module and a triple-axis accelerometer. The magnetometer/compass module measures the strength and direction of the magnetic field, offering insights into orientation and navigation. This information is valuable for applications requiring heading determination, direction sensing, or magnetometry.

The RGB camera utilized in the system is the uCAM-III (see Figure 12) by 4D systems. This camera is a versatile and integrated serial camera module designed for embedded imaging applications. It can be easily attached to any host system requiring a video camera or a JPEG-compressed still camera. The camera's compact form factor includes a built-in lens and a 5-wire connector, which enables easy access to both power and serial data.

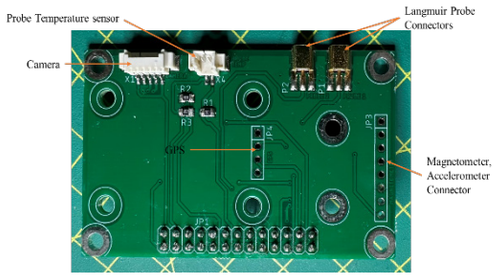

FIGURE 11. Auxiliary board top

Images provide an observatory view of the atmosphere's characteristics, cloud forms, and any unique phenomena observed during the measurements. The cloud movements, atmospheric structures, and the spatial distribution of mesosphere-related particles or components can all be studied through the analysis of these photographs. Images also assist in recognizing and recording any transitory events or atmospheric disturbances that may take place throughout the measurement campaign, resulting in a more thorough understanding of the behavior of the mesosphere.

FIGURE 12. uCAM III by 4D Systems

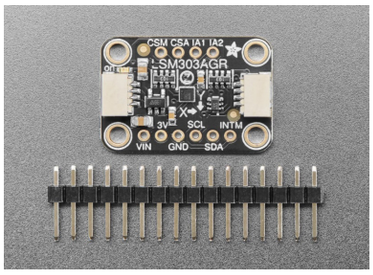

FIGURE 13. 3-axis magnetometer and accelerometer

The COTS sensor used to measure acceleration and magnetism is an ultralow-power high-performance system-in-package from ST Microelectronics, featuring a 3-axis digital linear accelerometer and a 3-axis digital magnetometer, specifically the LSM303AGR model (see Figure 13). This LSM303AGR includes an I²C serial bus interface that supports standard, fast mode, fast mode plus, and high-speed (100 kHz, 400 kHz, 1 MHz, and 3.4 MHz) and Serial Peripheral Interface (SPI). The LSM303AGR will be configured to generate an interrupt signal for free-fall, motion detection, and magnetic field detection.

Acceleration, or the rate of velocity change, is measured with an accelerometer. An accelerometer can offer useful information on the movement and variations in the acceleration of particles, such as atmospheric components or atmospheric disturbances, in the mesosphere layer. Acceleration measurements provide information on atmospheric dynamics, gravity wave propagation, and other mesospheric processes.

The magnetometer is used to gauge the magnetic field's intensity and direction. It is used to study the behavior of the Earth's magnetic field and its variations in the mesosphere layer. It aids in the investigation of the interactions between the magnetic field and atmospheric particles as well as the impact of external influences like solar activity on the magnetic properties of the mesosphere.

FIGURE 14. u-blox 6 GPS

As shown in Figure 14, the GPS is based on a low-cost, yet powerful GPS receiver and based on the u-blox 6 GPS chipset, which provides accurate and reliable positioning information with a 50-channel GPS receiver. It supports multiple positioning modes including GPS, Galileo, BeiDou, and QZSS. The module communicates with the host microcontroller using the serial UART protocol.

The utilization of GPS is crucial in in-situ measurements conducted in the mesosphere layer. GPS provides precise and accurate positioning information, enabling the determination of the exact location and altitude of the measurement of the Plasma probe. By incorporating GPS data, the measurements can be correlated with specific geographic coordinates and altitude levels in the mesosphere. This information is essential for accurately mapping the spatial distribution of atmospheric parameters. GPS data also aids in tracking the movement and trajectory of measurement instruments, allowing for better analysis and interpretation of the collected data.

Plasma probes consist of both positive and negative components. These probes are designed to measure specific plasma parameters. The positive probe is biased with a positive voltage relative to the surrounding plasma, attracting electrons and allowing for the measurement of electron current and related plasma properties. Similarly, the negative probe is biased with a negative voltage, repelling electrons but attracting positively charged ions, thereby enabling the measurement of ion current and associated plasma characteristics (Latif et al. 2020).

To facilitate data storage and analysis, the analog signals obtained from these plasma probes are converted into digital format. This conversion process ensures that the data can be effectively captured, processed, and stored. The digital data is then stored on an SD card for further analysis and interpretation.

The VHF Transceiver board is based on Owl by Skagmo Electronics (see Figure 15). It is small and lightweight with a high-performance radio transceiver. It is selected to handle VHF communication capabilities, enabling reliable two-way communication between the system and the ground station or other compatible receivers (Tømmer et al. 2015).

The primary function of this transceiver is to transmit telemetry, receive commands, and downlink payload data. This board incorporates the necessary circuitry, modulation schemes, and amplification to ensure efficient and accurate VHF communication.

The transceiver operates in a half-duplex mode, meaning it can either transmit or receive data packets at a given time. It employs audio frequency shift keying (AFSK) modulation to convert digital data into audio tones that can be transmitted over the radio waves. On the receiving end, the transceiver demodulates the received audio signals and processes them to extract the digital data packets.

This transceiver was selected due to the capability of providing AX.25 protocol. The AX.25 protocol transceiver plays a vital role in facilitating communication with the radio operators on the ground. It enables reliable and standardized packet radio communication, supporting the exchange of messages, data, and commands with the ground station radio operator (Parry, 1997).

FIGURE 15. VHF transceiver

A detailed study considering numerous crucial aspects must be conducted when calculating the communication link budget to ensure a strong and dependable communication link between the system and the ground station (Ya'acob et al. 2017). This thorough assessment takes important factors like power, gains, losses, and other characteristics into account, allowing for a precise assessment of the link's performance and viability. The equation for the RF link budget is as follows:

$$P_{RX} = P_{TX} - L_{TX} + G_{TX} - L_P + G_{RX} - L_{RX} \quad (1)$$

Where:

P_{Tx} is a transmit power.
L_{Tx} is a loss at transmitter, cable, connectors, etc.
G_{Tx} is a transmitter antenna gain.
L_p is a propagation loss.
G_{Rx} is a receiver antenna gain.
L_{Rx} is a loss at receiver, cable, connectors, etc.
P_{Rx} is a receive power.

Note that the first 3 terms of the equation equal the transmitter EIRP.

TABLE 4. System link budget

No	Parameters	Unit	Downlink/Uplink
1	Power Handling	dBm	33
2	Gain (> 0)	dBi	0
3	Sensitivity	dBm	-120
4	Rx Antenna Gain	dBi	1.8
5	Satellite Cable Loss	dB	1
6	Tx Power	dBm	37
7	Transmitter Gain	dBi	1.8
8	Path Loss	dB	117.178
Margin		dB	41.52

... cont.

Since identical transceiver and antenna were used for point-to-point communication with the distance between each other at 50 km apart. The calculated link margin as described in Table 4 indicates that the system will have a healthy link margin of 41.52 dB.

RESULT AND DISCUSSION

Figure 16 depicted as a result of the final assembly and integration process. It is illustrating the complete integration of PCBs in a stacked configuration, facilitated by spacers, and the interconnectivity achieved through the PC104 connector, encompassing power distribution, data transmission, and communication protocols.

The integrated electronic boards for the platform have gone through functional testing and have produced the intended results. The compact design accommodates the rocket's space limitations by ingeniously fitting complex components onto a small PCB measuring under 100 x 100 mm. Weighing just 0.5 kg, the platform consumes 0.8 W during idle and 1.3 W during transmission.

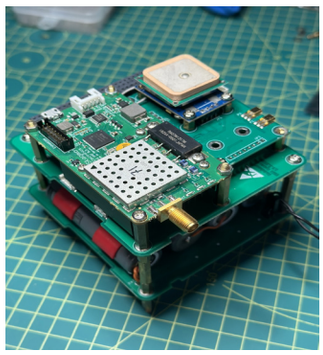

FIGURE 16. Complete assembled and integrated platform

The EPS subsystem produces the expected output voltages and includes a charging circuit to charge the battery. Based on Figure 8, Table 5 presents the results of the fixed 3.3V and 5V LDO voltage regulator circuit. The input voltage of 18V was applied to the regulators, producing an output voltage of 5V for the LDL1117S50R part and 3.3V for the LDL1117S33R.

TABLE 5. Result of fixed 3.3V and 5V LDO voltage regulator circuit

Input Voltage	Part Number	Output voltage
18V	LDL1117S50R	5V
18V	LDL1117S33R	3.3V

Table 6 displays the results of the L4931ABD voltage regulator under different inhibit conditions. With an input voltage of 16V (V_{BAT}), the L4931ABD33 outputs 3.3V and the L4931ABD50 outputs 5V when the inhibit signal is low. Both regulators output 0V when the inhibit signal is high.

TABLE 6. Result on controllable 3.3V and 5V LDO voltage regulator circuit

Input Voltage	Inhibit	Part Number	Output voltage
V_{BAT} @ 16V	Low	L4931ABD33	3.3 V
	Low	L4931ABD50	5 V
	High	L4931ABD33	0 V
	High	L4931ABD50	0 V

The battery pack, although seemingly over-designed, serves its purpose well. Power budget calculations confirm excess energy, with 82% of initial capacity remaining after a 10-minute test, allowing for higher-power payloads or extended mission durations.

The temperature sensor used in this circuit is a temperature-sensitive resistor (thermistor). Refer to Figure 17, 10k Ω thermistor (TH1) is connected in a voltage divider configuration with a fixed resistor (R2) of the same value. As temperature changes, the thermistor's resistance varies, altering the voltage across the junction, which can then be measured and correlated to the temperature.

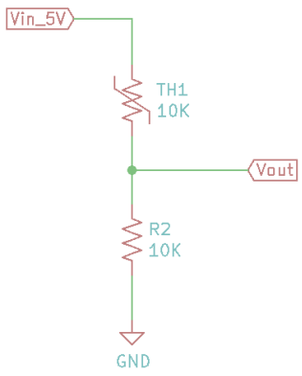

FIGURE 17. Voltage divider circuit

The battery temperature correlates with the voltage output from the voltage divider. The equation to correlate the voltage output as follows:

$$V_{out} = V_{in\_5V} \times \frac{R2}{TH1+R2} \quad (2)$$

Where:

V_{out} is the output voltage across the 10k resistor.
V_{in_5V} is the input voltage, which is 5V.
R2 is the resistance of the 10k resistor.
TH1 is the resistance of the thermistor in the divider.

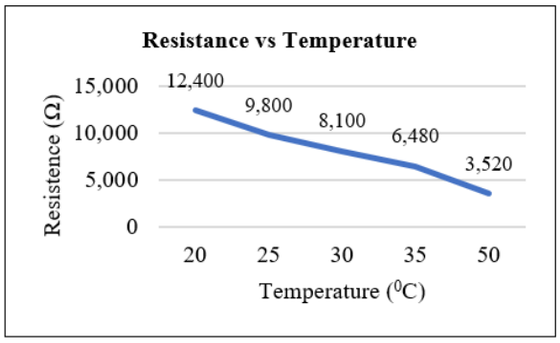

FIGURE 18. Resistance vs. temperature

As a result, a series of samples were collected, and their temperatures were validated using an external temperature sensor device placed at the same location as the thermistor. The recorded results can be found in Figure 18 and Table 7.

Table 7 describes the tolerance based on the percentage of the actual result compared to the datasheet of the temperature sensor.

TABLE 7. Result correlation of the output voltage and the measured temperature

No	Measured Temperature (°C)	Resistance value (Ω)	Tolerance (%)
1	20	12,400	0.7
2	25	9,800	2
3	30	8,100	0.5
4	35	6,480	0.8
5	50	3,520	2.3

The battery charger is based on the SEPIC circuit topology. It is based on the LT1513CRPBF component. It is a 500kHz current mode switching regulator specially configured to create a constant- or programmable-current/ constant-voltage battery charger. Table 8 and Figure 19 below shows the current drawn in relation to the fixed voltage of 5V while charging the battery from 14V to 16V.

TABLE 8. Current drawn in relation to the fixed voltage of 5V while charging the battery

No	Input Voltage (V)	Current (A)	Battery Voltage (V)
1	5V	0.6A	14V
2	5V	0.6A	14.5V
3	5V	0.4A	14.8V
4	5V	0.2A	15.5
5	5V	0.05A	16V

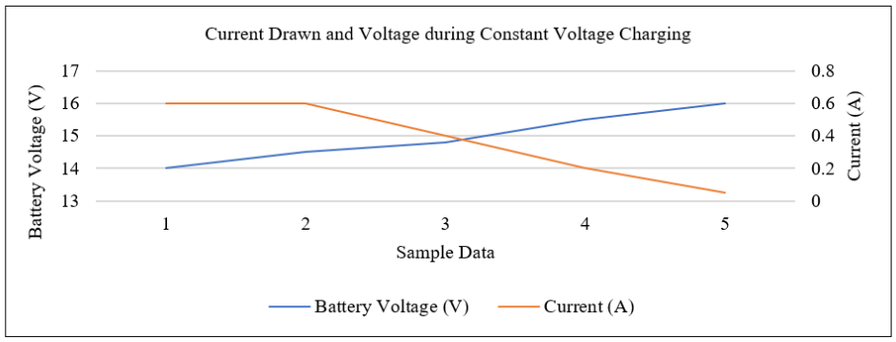

FIGURE 19. Current drawn and voltage during constant voltage charging

The choice of the ATmega2560 processor for the OBC board proves suitable, with embedded software performing well throughout testing. I²C and SPI protocols exhibit zero failures during short and endurance tests. Utilizing Arduino firmware simplifies programming, as accessible APIs replace custom driver development.

Developing applications with stringent timing requirements for this project requires using a Real-Time Operating System (RTOS) with task prioritization, as shown in Figure 20, real-time operating software flowchart. Task prioritization ensures timely performance by assigning higher priority to critical tasks. RTOS assigns higher numbers (in the circle Figure 20) to higher priority tasks, ensuring execution within specified timeframes. Equal numbers indicate equal priority.

As part of verification process is to validate that a product or system fulfills predetermined requirements and maintains fidelity to its designated design. Specifically, in this context, verification entails assessing the functionality and performance of the tested instrument. Emphasis is placed on ensuring the seamless operation of the instrument's operating software throughout the entirety of the testing phase, underscoring its stability and reliability as an integrated system. Verification on the integrity of the data transmission also needs to be validated. This is to ensure that the performance of the instrument as a complete system was tested and verified. To verify this, the instrument needs to go for endurance test. In this case, the instrument needs go for extensive testing for four 4 hours straight to ensure that it is capable to continued functions over long periods and the setup as shown is Figure 21.

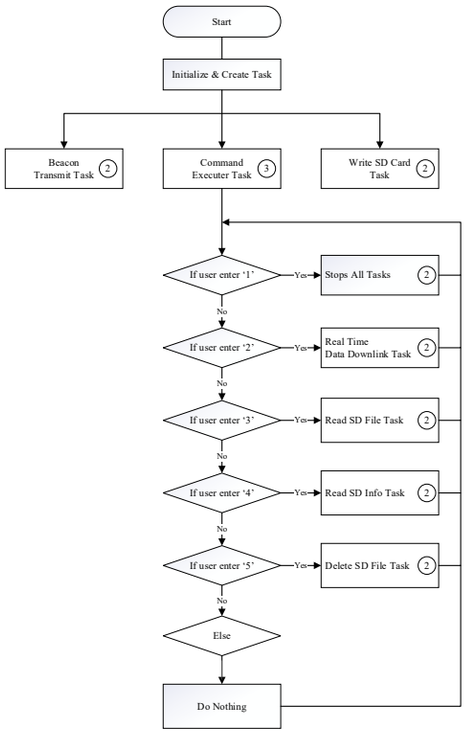

FIGURE 20. Realtime operating software flowchart

Result shown as in Table 9 and the sample outcome as shown in Figure 22. It was observed that the operating system produced real-time data transfer to the ground station terminal for the first three hours without any issues. For the last hour of testing, the real-time data transfer observed a delay of one second during the transmission. As part of the contingency and to support software redundancy systems, the file generation is automatic, which runs at a predetermined interval, guarantees system dependability and data retention. It provides practicality and redundancy by periodically producing files, which protects against any system failures. This strategy improves data continuity, reduces the likelihood of data loss, and strengthens the system's resiliency. While the operating software has been verified, the validation of data collected from the sensors remains pending.

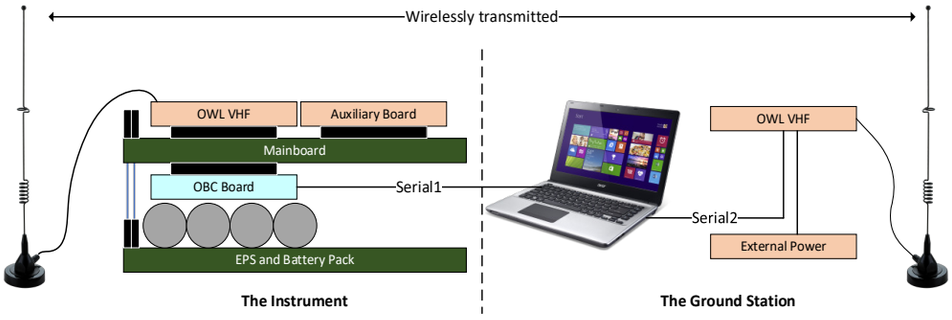

FIGURE 21. Endurance end to end test setup

```
OWL71>APOW1,WIDE1-1,WIDE2-1:2023/6/2 10:07:29
OWL71>APOW1,WIDE1-1,WIDE2-1:Accel (m/s^2): -0.06,2.28,9.72
OWL71>APOW1,WIDE1-1,WIDE2-1:Magnetic Field (uT): 5.55,9.18,20.10
OWL71>APOW1,WIDE1-1,WIDE2-1:Heading (Deg): 40.76
OWL71>APOW1,WIDE1-1,WIDE2-1:Temperature (C): 24.78
OWL71>APOW1,WIDE1-1,WIDE2-1:GPS: 5.147 100.494
OWL71>APOW1,WIDE1-1,WIDE2-1:TeNeP: 14
OWL71>APOW1,WIDE1-1,WIDE2-1:Battery: 4.9V

OWL71>APOW1,WIDE1-1,WIDE2-1:2023/6/2 10:07:30
OWL71>APOW1,WIDE1-1,WIDE2-1:Accel (m/s^2): -0.02,2.27,9.72
OWL71>APOW1,WIDE1-1,WIDE2-1:Magnetic Field (uT): 5.73,8.82,19.69
OWL71>APOW1,WIDE1-1,WIDE2-1:Heading (Deg): 38.62
OWL71>APOW1,WIDE1-1,WIDE2-1:Temperature (C): 24.78
OWL71>APOW1,WIDE1-1,WIDE2-1:GPS: 5.147 100.494
OWL71>APOW1,WIDE1-1,WIDE2-1:TeNeP: 14
OWL71>APOW1,WIDE1-1,WIDE2-1:Battery: 4.9V

OWL71>APOW1,WIDE1-1,WIDE2-1:2023/6/2 10:07:31
OWL71>APOW1,WIDE1-1,WIDE2-1:Accel (m/s^2): -0.06,2.26,9.70
OWL71>APOW1,WIDE1-1,WIDE2-1:Magnetic Field (uT): 5.45,9.27,19.80
OWL71>APOW1,WIDE1-1,WIDE2-1:Heading (Deg): 42.13
OWL71>APOW1,WIDE1-1,WIDE2-1:Temperature (C): 24.78
OWL71>APOW1,WIDE1-1,WIDE2-1:GPS: 5.147 100.494
OWL71>APOW1,WIDE1-1,WIDE2-1:TeNeP:14
OWL71>APOW1,WIDE1-1,WIDE2-1:Battery: 4.9V

OWL71>APOW1,WIDE1-1,WIDE2-1:2023/6/2 10:07:32
OWL71>APOW1,WIDE1-1,WIDE2-1:Accel (m/s^2): -0.07,2.24,9.69
OWL71>APOW1,WIDE1-1,WIDE2-1:Magnetic Field (uT): 5.64,9.18,19.90
OWL71>APOW1,WIDE1-1,WIDE2-1:Heading (Deg): 40.69
OWL71>APOW1,WIDE1-1,WIDE2-1:Temperature (C): 24.78
OWL71>APOW1,WIDE1-1,WIDE2-1:GPS: 5.146 100.494
OWL71>APOW1,WIDE1-1,WIDE2-1:TeNeP: 14
OWL71>APOW1,WIDE1-1,WIDE2-1:Battery: 4.9V

OWL71>APOW1,WIDE1-1,WIDE2-1:2023/6/2 10:07:33
OWL71>APOW1,WIDE1-1,WIDE2-1:Accel (m/s^2): -0.08,2.24,9.64
OWL71>APOW1,WIDE1-1,WIDE2-1:Magnetic Field (uT): 5.64,9.18,20.10
OWL71>APOW1,WIDE1-1,WIDE2-1:Heading (Deg): 41.20
OWL71>APOW1,WIDE1-1,WIDE2-1:Temperature (C): 24.87
OWL71>APOW1,WIDE1-1,WIDE2-1:GPS: 5.146 100.494
OWL71>APOW1,WIDE1-1,WIDE2-1:TeNeP: 14
OWL71>APOW1,WIDE1-1,WIDE2-1:Battery: 4.9V

OWL71>APOW1,WIDE1-1,WIDE2-1:2023/6/2 10:07:34
OWL71>APOW1,WIDE1-1,WIDE2-1:Accel (m/s^2): -0.02,2.24,9.67
OWL71>APOW1,WIDE1-1,WIDE2-1:Magnetic Field (uT): 5.27,9.27,20.10
OWL71>APOW1,WIDE1-1,WIDE2-1:Heading (Deg): 43.27
OWL71>APOW1,WIDE1-1,WIDE2-1:Temperature (C): 24.96
OWL71>APOW1,WIDE1-1,WIDE2-1:GPS: 5.147 100.494
OWL71>APOW1,WIDE1-1,WIDE2-1:TeNeP: 14
OWL71>APOW1,WIDE1-1,WIDE2-1:Battery: 4.9V
```

FIGURE 22. Sample of real time data downlink task

However, as the sensors are not developed from the ground up, preliminary assumptions regarding the data can be validated using the datasheets provided by the manufacturer.

Furthermore, future work is recommended to ensure the validation of sensor data. This endurance trial confirmed the platform's ability to transmit sensor data in real-time according to the predetermined interval set in the OBC.

TABLE 9. Endurance test outcome

Test Duration	Time (HH:MM)	Outcome
4 Hours	00:00 – 01:00	Real-Time Data Transfer
	01:00 – 02:00	Real-Time Data Transfer
	02:00 – 03:00	Real-Time Data Transfer
	03:00 – 04:00	Delay of 1 second in data transfer

In conclusion, the platform effectively demonstrates its functional capabilities for in-orbit testing, showcasing innovative design and successful subsystem integration.

As for the topic of discussion, the remaining required tests include environmental testing and long-range communication testing. The vibration test, which is part of the environmental testing activity, will ensure the platform will mechanically survive and will be able to operate effectively after going through the harsh environment due to rocket engine vibrations. Meanwhile, the thermal vacuum test will verify the platform's ability to operate under similar temperature, pressure, and humidity conditions as those found in the mesosphere and ionosphere layers. The long-range communication test will involve the verification of the link budget. This can be done either by conducting the communication transceiver device on its own or integrating it as a complete system. Currently, the platform's mechanical design can accommodate a sounding rocket example from ISRO (RH-200), but customization of the bracket is required for full integration with the platform. This customization will be different and will tailor the design according to the type of sounding rocket. Moreover, For future work in the field of data collection for actual plasma probe sensors such as electron temperature and density probe (TeNeP) (Latif et al. 2020), The platform needs to ensure its compatibility in terms of signal transmission and the platform's data acquisition system must be collected correctly. Secondly, testing the performance of the connection between the sensor and the platform is an important step. This validation process should focus on making sure there are no problems that could cause data to get worse. This will make sure that the quality and integrity of the samples collected do not change. Lastly, it is important to keep the sensor's accuracy over time.

CONCLUSION

In summary, this paper introduces a system that offers unique access to the mesosphere and Ionosphere layer. This advanced system enables real-time communication between the payload operation and the ground station operator, enabling efficient data transfer.

These developments are aimed at improving performance and ensuring seamless operation to further improve the system, continuing efforts are focused on minimizing weight and refining the flight operating software.

By providing an instrument to discover the mesosphere layer and enabling real-time access, this system opens new opportunities for scientific research. The continuous improvement of the system's weight and flight operating system will contribute to its overall efficiency, allowing for an enhanced understanding of the mesosphere layer and its dynamics.

ACKNOWLEDGEMENT

This work was supported by the "Ministry of Higher Education Malaysia for Fundamental Research Grant Scheme with Project Code2: FRGS/1/2020/STG07/USM/03/3."

DECLARATION OF COMPETING INTEREST

None.

REFERENCES

Amatucci, W. E., Schuck, P. W., Walker, D. N., Kintner, P. M., Powell, S., Holback, B., & Leonhardt, D. 2001. Contamination-free sounding rocket Langmuir probe. *Review of Scientific Instruments 72*(4): 2052–2057.

Amos, B. 2020. *Hands-On RTOS with Microcontrollers: Building real-time embedded systems using FreeRTOS, STM32 MCUs, and SEGGER debug tools*. Packt Publishing Ltd.

Astafyeva, E. 2019) Ionospheric Detection of Natural Hazards. *Reviews of Geophysics 57*(4): 1265–1288. https://doi.org/10.1029/2019RG000668

Christe, S., Zeiger, B., Pfaff, R., & Garcia, M. 2016. Introduction to the Special Issue on Sounding Rockets and Instrumentation. *Journal of Astronomical Instrumentation 5*(01): 1602001. https://doi.

org/10.1142/S2251171716020013

Dahbi, S., Aziz, A., Zouggar, S., El Hafyani, M., Morocco, O., Hanafi, A., Karim, M., Latachi, I., & Rachidi, T. 2017. Power budget analysis for a LEO polar orbiting nano-satellite. *2017 International Conference on Advanced Technologies for Signal and Image Processing (ATSIP):* 1–6.

Ejiri, M. K., Katsuragawa, M., Hashimoto, A., Kobayashi, S., Tsuda, T. T., & Nakamura, T. (n.d.). *Development of a resonance scattering lidar for simultaneous measurement of meteoric metal atom and ion in the mesosphere and thermosphere*.

Kim, J.-H., Jee, G., Choi, H., Kim, B.-M., & Kim, S.-J. 2020. Vertical structures of temperature and ozone changes in the stratosphere and mesosphere during stratospheric sudden warmings.

Latif, M. A. A., Lam, K. S., Thaheer, A. S. M., Ismail, N. A., Oyama, K.-I., Fang, H. K., & Yusoff, S. H. M. 2020. Preliminary design of MYSat payload: Electron temperature and density probe (TeNeP) generator circuit. *AIP Conference Proceedings 2226*(1).

Liu, T., Yang, G., Zhao, Z., Liu, Y., Zhou, C., Jiang, C., Ni, B., Hu, Y., & Zhu, P. 2020. Design of multifunctional mesosphere-ionosphere sounding system and preliminary results. *Sensors 20*(9): 2664.

Mahoudian, A., Patra, S., Sadeghi Kia, F., & Aliparast, P. (2020). First mesospheric in-situ measurement in Iran using sounding rockets and plasma impedance probe (PIP). *Journal of the Earth and Space Physics 45*(4): 237–244. https://doi.org/10.22059/jesphys.2019.269440.1007063

Meriwether, J. W., & Gardner, C. S. 2000. A review of the mesosphere inversion layer phenomenon. *Journal of Geophysical Research: Atmospheres 105*(D10): 12405–12416.

Meriwether, J. W., & Gerrard, A. J. 2004. Mesosphere inversion layers and stratosphere temperature enhancements. *Reviews of Geophysics 42*(3). https://doi.org/https://doi.org/10.1029/2003RG000133

Nieto-Peroy, C., & Emami, M. R. 2019. CubeSat mission: From design to operation. *Applied Sciences 9*(15): 3110.

Noga, T., & Puri, R. 2020. Microgravity, atmosphere sounding, astronomy, technology validation - an overview of suborbital rockets' missions and payloads. *International Journal of Space Science and Engineering 6*(2): 179–208. https://doi.org/10.1504/IJSPACESE.2020.110365

Parry, R. R. 1997. AX. 25 [data link layer protocol for packet radio networks]. *IEEE Potentials 16*(3): 14–16.

Shiro, B., Freund, F., Cagle, Y., Pilorz, S., Hollis-Watts, P., & Windsor, C. 2012. Measuring Ion Currents and Electric Fields Caused by Earthquakes, Volcanoes, and Lightning in the Mesosphere. *Technology 11*: 12.

Tømmer, M., Birkeland, R., Gjersvik, A., Stein, T. A., Vestnes, F., Skagmo, J. P., Kvamtrø, K. M., Eckholdt, F., Alstad, T., Grande, J., & others. (2015). Testing of radio communication subsystems for the NUTS CubeSat on a meteorological balloon flight from Andøya in 2014. *Proceedings of the 22nd ESA Symposium on European Rocket and Balloon Programs and Related Research, Tromson, Norway*, 479–484.

Uma, K. N., Das, S. S., Adimurthy, V., & Ramachandran, R. 2024. An empirical model for the tropical Indian region using in-situ and space-borne observations taking into account of tropical oscillations. *Advances in Space Research*.

Ward, H. 2023. The Real-Time Clock and the DS3231. In *Introductory Programs with the 32-bit PIC Microcontroller: A Line-by-Line Code Analysis and Reference Guide for Embedded Programming in C* (pp. 465–557). Springer.

Ya'acob, N., Johari, J., Zolkapli, M., Yusof, A. L., Sarnin, S. S., & Naim, N. F. 2017. Link budget calculator system for satellite communication. *2017 International Conference on Electrical, Electronics and System Engineering (ICEESE):* 115–119.

Yao, M., Zhang, L., Deng, X., Bai, B., Wu, W., Zhou, M., Li, H., & Lu, Z. 2013. System design of the prototype incoherent scatter radar at Nanchang University. *IEEE Geoscience and Remote Sensing Letters 11*(1): 352–356.